An Adaptive Nonlocal Regularized Shadow Removal Method for Aerial Remote Sensing Images

Huifang Li, Liangpei Zhang, *Senior Member, IEEE*, and Huanfeng Shen, *Member, IEEE*

***Abstract*—Shadows are evident in most aerial images with high resolutions, particularly in urban scenes, and their existence obstructs the image interpretation and the following application, such as classification and target detection. Most current shadow removal methods were proposed for natural images, whereas shadows in remote sensing images show distinct characteristics. We have therefore analyzed the characteristics of shadows in aerial images, and in this paper, we propose a new shadow removal method for aerial images, using nonlocal (NL) operators. In the proposed method, the soft shadow is introduced to replace the traditional binary hard shadow. NL operators are used to regularize the shadow scale and the updated shadow-free image. Furthermore, a spatially adaptive NL regularization is introduced to handle compound shadows. The combination of the soft shadow and NL operators yields satisfying shadow-free results, preserving textures and holding regular color. Different types of shadowed aerial images are employed to verify the proposed method, and the results are compared with two other methods. The experimental results confirm the validity of the proposed method and the advantage of the soft-shadow approach.**

***Index Terms*—Aerial images, nonlocal (NL) operators, shadow removal, soft shadow, spatially adaptive.**

I. INTRODUCTION

SHADOWS exist in most aerial remote sensing images with high resolutions. The properties of a shadow, such as the size, the shape, and the direction, are important factors when reconstructing a 3-D model of the corresponding object, e.g., a building. However, the reduction or even loss of radiance in the shadow regions causes problems in mapping, target detection, and some other applications. Therefore, shadow removal is an essential preprocessing step in the interpretation of remote sensing images. There have been many studies of shadow removal for natural images but few for remote sensing images. We intend to analyze the characteristics of shadows in aerial remote sensing images and propose a feasible method to remove shadows from these images.

Generally, shadow removal involves two procedures, i.e., detection and compensation. The latter aspect is the core of our paper, although a detection result with high accuracy is important to the final shadow compensation (SC). Current image-based shadow detection (SD) methods can be divided into two types, i.e., unsupervised detection and supervised detection. No samples are needed for unsupervised detection, as the shadows are extracted by some prior characteristics, such as low intensity in a single-band image. Recently, a blackbody radiator model [1] has been put forward to detect shadows, which is based on the physical properties of a blackbody radiator, i.e., the temperature of direct light differs from the temperature of scattered light. For multiband images, invariant color spaces are often used to stress shadows, for shadow regions hold higher hue and lower intensity than nonshadow regions [2]–[4]. In supervised SD methods, samples are trained to construct the feature sets representing shadows and nonshadows. Shadows are then distinguished from the nonshadows by measuring the differences between each pixel and each feature set. Classifiers, such as Support Vector Machine (SVM), assisted by various mathematical morphological operators, are often taken as the measurements [5], [6]. All these methods distinguish shadows and nonshadows absolutely, resulting in a binary mask with a hard edge. However, the hard shadow is not sufficient to depict shadows in high-resolution images, due to the nonuniform distribution and the existence of penumbras. Therefore, the soft shadow, in contrast with the binary hard shadow, has been proposed in some literatures, which define the shadow by the degree to which each pixel belongs to it. Thus, the soft shadow depicts shadows more distinctly than the hard shadow and has advantages in solving nonuniform shadow problems. The degree to which each pixel belongs to the shadow is measured by different means, such as the distance between the pixel and the feature set [7], the morphological shadow index (MBI) [8], and segmenting the shadow pixels by subjective thresholding based on a histogram of shadow pixels [9]. The distance measure is applicable for a pure shadow, which only covers one kind of land surface. The MBI is unsupervised and efficient but fails to detect those shadow pixels surrounded by darker pixels. Levels in the subjective thresholding method are discrete and are not enough for the nonlocal (NL) operators. Here, we obtain the soft shadow by image matting [10], and we further investigate the effectiveness of this approach in this paper.

There are two kinds of SC methods according to the computing domain, i.e., SCs in the intensity and gradient domains. The SC methods in the intensity domain include two different modes. One takes advantage of the spatial similarity, restoring the shadow regions by their surrounding nonshadow regions.

Manuscript received August 14, 2012; revised November 5, 2012; accepted December 18, 2012. This work was supported in part by the Major State Basic Research Development Program of China (973 Program) under Grant 2011CB707103, by the National Natural Science Foundation of China under Grant 40930532 and Grant 40971220, and by Hubei Natural Science Foundation under Grant 2011CDA096.

H. Li and L. Zhang are with the State Key Laboratory of Information Engineering in Surveying, Mapping, and Remote Sensing, Wuhan University, Wuhan 430079, China (e-mail: l.huifang10@gmail.com; zlp62@whu.edu.cn).

H. Shen is with the School of Resource and Environmental Science, Wuhan University, Wuhan 430079, China, and also with the State Key Laboratory of Information Engineering in Surveying, Mapping, and Remote Sensing, Wuhan University, Wuhan 430079, China (e-mail: shenhf@whu.edu.cn).

Color versions of one or more of the figures in this paper are available online at http://ieeexplore.ieee.org.

Digital Object Identifier 10.1109/TGRS.2012.2236562

Paired regions with the same land surface are usually needed as the prior through manual selection. The relationship between the intensity of the paired shadows and nonshadows is then constructed by a computation method such as linear regression [11] or histogram statistic [2], [6], [12]. The other mode of SC in the intensity domain is based on the definition of the shadow image, i.e., the product of a shadow-free image and a shadow scale. Therefore, estimating the shadow scale of a shadow image is the essential step in removing shadows. Based on the spatial smoothness of the shadow scale, a thin-plate function has been used to obtain the final shadow scale in some literature [5], [13], [14]. For textural images, anchor points are selected to maintain the textures in the shadows [5]. However, the spatial smoothness assumption is false when the shadows are compound, i.e., composed of land surfaces with great differences. Thus, the thin-plate function cannot simulate this kind of complex situation very well.

A representative SC method in the gradient domain is the Poisson method, which reconstructs a shadow-free image based on the corrected gradients through the Poisson equation [15]–[17]. However, the results of this method are highly reliant on the SD results. Inaccurate location of shadows will lead to unexpected artifacts, i.e., the residual shadow edges. Moreover, the whole input image is reconstructed, without maintaining the original nonshadow regions. For that reason, a serious color cast will appear in the result if the corrected gradient is significantly wrong, e.g., when many pixels with zero intensity (0-pixels) exist in the shadow.

Consequently, we conclude that there are four main problems with removing shadows in aerial remote sensing images:

1) The 0-pixels commonly exist in dark shadows, which would cause a serious restoration error and color cast in the result.
2) Large shadows are compound, i.e., multiple land surfaces appear in the same shadow, so that textures and edges would be blurred if the spatial characteristics are ignored.
3) Shadows are nonuniform, i.e., the closer the surface is to the occlusion, the darker the corresponding shadow is. Algorithms will fail if all the shadow pixels are equally treated.
4) For the high-spatial-resolution shadowed image, if the influence of penumbras is not considered, residual fake edges will appear in the final results.

To solve the aforementioned four problems, this paper presents a new adaptive NL regularized shadow removal method for aerial images in the intensity domain, compensating shadows while maintaining nonshadows, based on an analysis of the characteristics of shadows. NL operators differ from the traditional image processing methods using local computation over a time–frequency or multiscale domain. They respect edges and textures better by employing pixels arbitrarily far from the central pixel [18]–[22]. This paper explores the advantages of NL operators. Following the traditional shadow removal methods, two steps, i.e., SD and SC, are included in the proposed method. Image matting is used for detecting soft shadows, and a NL regularized energy function, including one fidelity item and two NL regularized items, is proposed to complete the SC. Penumbras and nonuniform shadows are supposed to be well delineated by soft shadows.

The second section of this paper discusses image matting and the effect of soft shadows. Details of the NL regularized SC method, including the spatially adaptive strategy particularly for compound shadows, are given in the third section. The mechanism of the proposed NL method for solving the four problems of shadow removal is also discussed in this section. Three different types of aerial image are employed to verify the validity of the proposed method, and the results are exhibited in the fourth section. The influences of the initial markings and parameter settings on the SD and the compensation are also discussed in this section.

II. SOFT-SHADOW DETECTION

As mentioned before, most SD methods distinguish shadow and nonshadow absolutely. Exceptionally, the shadow matting method derives the concept of shadow probability, which is defined by a weighted color distance in natural images [7]. The shadow probability is pixelwise, and it defines the shadow relatively. Each pixel is encoded by a probability value to measure the degree to which it belongs to the shadow. The shadow is soft rather than hard. This concept corresponds with the existence of penumbras. The penumbra is the transition part from a shadow region to a nonshadow region. According to the calculation method introduced in [23], the width of the penumbra might be more than two or three pixels in a high-resolution aerial image. Therefore, the impact of the penumbra cannot be ignored in aerial remote sensing images. In the shadow probability map, one pixel should have a value of 1 if it belongs to the umbra, a value of 0 if it belongs to the nonshadow, and a value between 0 and 1 if it belongs to the penumbra. The soft-shadow concept is used in the proposed method. However, shadows in natural images are usually unitary, whereas shadows in aerial images are usually compound, i.e., each shadow is composed of numbers of different types of surfaces. Thus, the original definition in [7] is inappropriate for aerial images. Therefore, we have to define the shadow probability in another way. Here, image matting is used for the detection of soft shadows.

Image matting aims to extract a foreground object from an image, based on limited user input, as well as estimating the foreground opacity (“alpha matte”) [10]. Following the description in [10], the color of the ith pixel is assumed to be a linear combination of the corresponding foreground and background colors, i.e.,

$$I_i = \alpha_i G_i + (1 - \alpha_i) B_i, \quad \alpha \in [0, 1] \tag{1}$$

where G_i and B_i denote the foreground and the background, respectively, and α_i is the pixel’s alpha matte. A closed-form solution to natural image matting is presented by optimizing the cost function, i.e.,

$$\alpha = \arg\min \alpha^T L \alpha + \lambda(\alpha^T - b_S^T) D_S (\alpha - b_S) \tag{2}$$

where matrix L is defined as the *matting Laplacian*, λ is some large number and set 100 as introduced in [10], D_S is a diagonal matrix whose diagonal elements are 1 for constrained pixels and 0 for all other pixels, and b_S is the vector containing the specified alpha values for the constrained pixels and 0 for all other pixels. High-quality mattes were obtained by testing this method on many natural images. Moreover, when the foreground contains two or more types of materials, this method also works well. Here, for detecting the soft shadow, we suppose that the shadow is the foreground and the nonshadow is the background. Thus, the matte can locate the soft shadow relatively, and the normalized entry of each pixel represents the rough probability of it belonging to the absolute shadow, i.e., $p_s = \alpha$. We will discuss the validity of image matting for SD in the experimental part.

III. IMAGING MODEL FOR SHADOWED AERIAL IMAGES

For an aerial shadow image, intensity $I(x)$ can be assumed to be composed of three components, i.e., albedo $R(x)$, illumination $L(x)$, and the shadow scale $S(x)$. Albedo $R(x)$ is an invariant, which is only related to the physical property of the surface. Illumination $L(x)$ is usually assumed to be spatially smooth, without intensity leaps [24]–[26]. Intensity leaps in a shadow image are only attributed to the shadow scale component. Therefore, the formation for a shadow image can be simplified as

$$I(x) = F(x) \cdot S(x) \tag{3}$$

where $F(x) = R(x) \cdot L(x)$ denotes the shadow-free image with the influence of the illumination. In the log domain, (3) is reformulated as

$$i(x) = f(x) + s(x) \tag{4}$$

where i, f, and s are the logarithms of I, F, and S, respectively. The distribution of the shadow scale is consistent with the soft shadow, while the entry of the shadow scale is close to the complement of the shadow probability in the [0, 1] range. This suggests that a shadow pixel with high shadow probability has a low shadow scale factor. We intend to take advantage of the consistency of the distribution of these two variables and put NL operators on the shadow scale.

IV. NL REGULARIZED SHADOW COMPENSATION METHOD

An energy function, including three items for SC, is constructed. The first item ensures the approximation of the result to the predicted shadow-free image. The second and third items are NL operators, used to constrain both the shadow scale and the updated shadow-free image. The regularization parameter of the third item is pixelwise adaptive, which solves the problem of nonuniform shadows. Furthermore, clustering is performed in the compound shadow region to treat different surfaces differently, which retains the edges and the textures in the shadow region.

A. Fidelity Item

The proposed NLSC method follows the rule of maintaining the nonshadow regions while compensating for the lost intensity in the shadow regions. Therefore, the data fidelity item, making the result approximate the predicted shadow-free image $\hat{f}$, is included in the energy function. In the nonshadow regions, the original intensities are maintained; in the shadow regions, the predicted shadow-free image is estimated by the color transfer, as introduced in [7] and [27]–[29]. The color transfer synthesizes a region by transferring some aspects of the distribution of the data points in color space from a source region to a target region. In our method, the source region is the shadow, and the target region is the nonshadow region selected by the user, which belongs to a similar surface type as the shadow region. Let $T(i(x))$ be the transformed intensity, which should be nonnegative, and ς and $\bar{\varsigma}$ denote the shadow and nonshadow regions, respectively. Let μ_ς and σ_ς be the mean and the standard deviation of ς, i.e., $\varsigma \sim N(\mu_\varsigma, \sigma_\varsigma^2)$; similarly, let $\mu_{\bar{\varsigma}}$ and $\sigma_{\bar{\varsigma}}$ be the mean and the standard deviation of $\bar{\varsigma}$, i.e., $\bar{\varsigma} \sim N(\mu_{\bar{\varsigma}}, \sigma_{\bar{\varsigma}}^2)$. Then

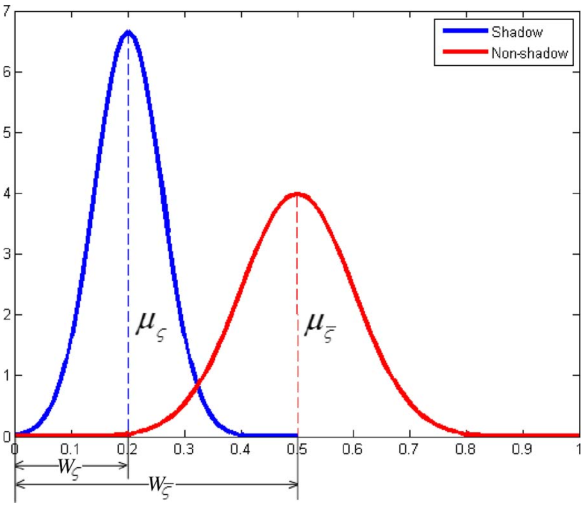

Fig. 1. Gaussian distribution of shadows and nonshadows.

$$T\left(i(x)\right) = \mu_{\bar{\varsigma}} + \frac{\sigma_{\bar{\varsigma}}}{\sigma_\varsigma}\left(i(x) - \mu_\varsigma\right). \tag{5}$$

For all shadow pixels, no matter if they have low or zero intensities, the transformed intensities based on (5) can be assured to be nonnegative. This transformation is a monotone increasing function, and $i(x)$ is nonnegative. Thus, if only $T(0) = \mu_{\bar{\varsigma}} - (\sigma_{\bar{\varsigma}}/\sigma_\varsigma) \cdot \mu_\varsigma \geq 0$, i.e., $(\mu_{\bar{\varsigma}}/\mu_\varsigma) \geq (\sigma_{\bar{\varsigma}}/\sigma_\varsigma)$, the $T(\cdot)$ function is nonnegative. Supposing an extreme condition, the minimum values of the shadow and nonshadow regions are both zero. In Fig. 1, the blue curve represents the distribution of shadow pixels, and the red one represents the distribution of nonshadow pixels, where $\mu_{\bar{\varsigma}} > \mu_\varsigma$. W_ς and $W_{\bar{\varsigma}}$ are the approximate half-widths of these two Gaussian peaks, and it can be then seen that $\mu_\varsigma = W_\varsigma \approx 2\sigma_\varsigma$ and $\mu_{\bar{\varsigma}} = W_{\bar{\varsigma}} \approx 3\sigma_{\bar{\varsigma}} \Rightarrow (\mu_{\bar{\varsigma}}/\mu_\varsigma) \approx (3\sigma_{\bar{\varsigma}}/2\sigma_\varsigma) > (\sigma_{\bar{\varsigma}}/\sigma_\varsigma)$. In most cases, the minimum of the nonshadow regions is larger than zero, i.e., $W_{\bar{\varsigma}} > 3\sigma_{\bar{\varsigma}}$; thus, this inequality is a necessary condition for $T(\cdot) \geq 0$. Therefore, this intensity transformation is not limited to the nonzero pixels, and it also works when some 0-pixels exist in the shadow regions.

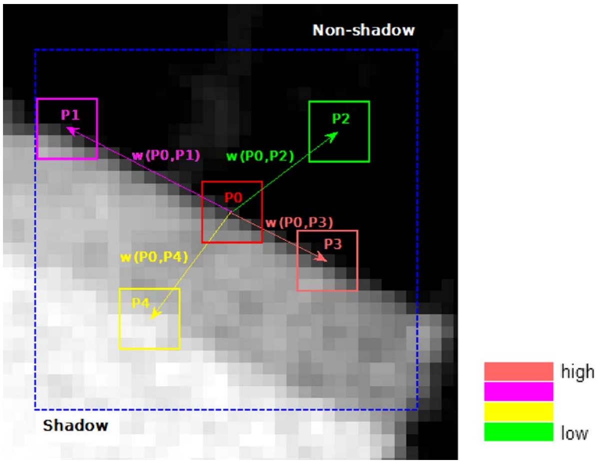

Fig. 2. NL weights.

Integrating the shadow probability, the original intensity, and the transformed intensity, the predicted shadow-free image $\hat{f}$ can be expressed as

$$\hat{f}(x) = i(x)\left(1 - p_s(x)\right) + T\left(i(x)\right) p_s(x). \tag{6}$$

The data fidelity item is constructed by the $L2$-norm, i.e.,

$$\kappa(f) = \sum_{\Omega} \|f - \hat{f}\|_{L2}^2. \tag{7}$$

B. NL Operators in Shadow Compensation

NL operators take advantage of pixels arbitrarily far away from the central pixel. Different weights based on the structural similarity between patches are arranged for the involved pixels. The structural similarity is usually measured by the distances in the gray and spatial domains. Let $\Omega \subset \mathbf{R}^n$, $x, y \in \Omega$, and $v(x)$ be a real function. The weight between x and y is defined by the following formula:

$$w(x,y) = \exp\left(-\frac{\left(G_a \left|v(x+.) - v(y+.)\right|^2\right)(0)}{h^2}\right) \tag{8}$$

where G_a is a Gaussian kernel with the standard deviation a, and h is a filtering parameter, which corresponds to the noise level. The weights are nonnegative and symmetric, i.e., $w(x,y) \geq 0$ and $w(x,y) = w(y,x)$. Fig. 2 shows the structural elements and the weights between the central and surrounding pixels. Pixels close to the central pixel and having a similar structure to it are assigned high weights. In contrast, low weights are assigned to those pixels far away from and different from the central pixel.

Two types of regularizing NL functions were proposed in [21]. One type is based on the NL gradient, which is isotropic; the other is based on differences, which is anisotropic. Here, we use the first type. The NL gradient $\nabla_w v(x) : \Omega \to \Omega \times \Omega$ is defined as the vector of all the partial derivatives, i.e.,

$$\nabla_w v(x) := \left(v(y) - v(x)\right)\sqrt{w(x,y)}. \tag{9}$$

The gradient-based NL function is

$$\begin{aligned} J(v) &= \int_{\Omega} \phi\left(|\nabla_w v|^2\right) dx \\ &= \int_{\Omega} \phi\left(\int_{\Omega} \left(v(y) - v(x)\right)^2 w(x,y) dy\right) dx \end{aligned} \tag{10}$$

where $\phi(\cdot)$ is a positive function. Here, we use the quadratic NL Laplacian prior, setting $\phi(s) = s$, and then, the discretization of (10) can be written as

$$J(v) = \sum_{\Omega} |\nabla_w v|^2 = \sum_{x \in \Omega} \sum_{y \in x^{\mathrm{NL}}} \left(v(y) - v(x)\right)^2 w(x,y) \tag{11}$$

where x^{NL} denotes the NL neighbors around x.

1) NL Regularization for the Shadow Scale:

Intensity leaps in a shadow image are attributed to the shadow scale, which is regionally smooth. The inner and outer parts of the shadow scale are both smooth, whereas the transition parts from the shadow to the nonshadow, i.e., the penumbra regions, depict the shadow edges. In order to remove shadow edges without residues, the soft edges should be maintained in the shadow scale. The NL operator is used to regularize the shadow scale to ensure the regional smoothness and preserve the soft edges. Considering the consistency of the shadow scale and the soft shadow, the NL weights in the shadow scale are calculated based on the soft shadow, as (12) shows. The NL regularization for the shadow scale is expressed as (13). Thus, the spatial smoothness of the homogeneous regions is ensured while retaining the textures and the edges, i.e.,

$$w_s(x,y) = \exp\left(-\frac{\left(G_a \left|p_s(x+.) - p_s(y+.)\right|^2\right)(0)}{h^2}\right) \tag{12}$$

$$\begin{aligned} J(s) &= \sum_{\Omega} |\nabla_{w_s} s|^2 \\ &= \sum_{x \in \Omega} \sum_{y \in x^{\mathrm{NL}}} \left(s(y) - s(x)\right)^2 w_s(x,y), \\ s &= i - f \end{aligned} \tag{13}$$

where s represents the shadow scale in the logarithm domain, w_s is the NL weight calculated based on the soft shadow, Ω denotes the total image region, and x^{NL} denotes the NL neighbors around x.

2) NL Regularization for the Updated Shadow-Free Image:

Abundant textures and some noise exist in the shadow regions. Thus, it is reasonable to regularize the shadow-free image by the NL Laplacian prior. Since the shadow-free image f is unknown, the weights are calculated based on the predicted shadow-free image $\hat{f}$ as follows:

$$w_f(x,y) = \exp\left(-\frac{\left(G_a \left|\hat{f}(x+.) - \hat{f}(y+.)\right|^2\right)(0)}{h^2}\right). \tag{14}$$

Then, the NL item for the shadow-free image is expressed as

$$J(f) = \sum_{\Omega} |\nabla_{w_f} f|^2 = \sum_{x\in\Omega} \sum_{y\in x^{\mathrm{NL}}} (f(y) - f(x))^2 \, w_f(x,y). \tag{15}$$

Consequently, the NLSC model is constructed as

$$E(f) = \kappa(f) + \lambda_s \cdot J(s) + \lambda_t \cdot J(f) \tag{16}$$

where λ_s and λ_t are the regularization parameters used for balancing the contribution of each item. Through minimizing the energy function, we can obtain the shadow-free image by the following formula:

$$f = \arg\min_f \sum_{\Omega} \left[\|f - \hat{f}\|_{L2}^2 + \lambda_s \cdot \sum_{y\in x^{\mathrm{NL}}} (s(x) - s(y))^2 \times w_s(x,y) + \lambda_t \cdot \sum_{y\in x^{\mathrm{NL}}} (f(x) - f(y))^2 \, w_f(x,y) \right]. \tag{17}$$

The energy function is quadratic; thus, its derivative $(\partial E/\partial f) = 0$ is linear. We implement the simple iterative Gauss–Seidel algorithm to solve the linear problem [7].

3) Parameter Selection: As mentioned before, in the soft-shadow image, a small entry represents a low shadow probability, and in contrast, a large entry represents a high shadow probability. Correspondingly, in the spatial domain, pixels with nonzero and low entries locate in the penumbra, pixels with high entries locate in the umbra, and pixels with zero entries represent the nonshadow. In order to get rid of the residual fake edges in the resulting shadow-free image, the second NL item should contribute more than the first NL item around the penumbra. This indicates the negative correlation between the regularization parameter λ_t and the entry of the soft shadow p_s. Thus, parameter λ_t can be adaptively set according to the shadow probability. Here, we take the negative exponent function to simulate the negative correlation, i.e.,

$$\lambda_t = c_1 \cdot \exp(-c_2 \cdot p_s) \tag{18}$$

where c_1 and c_2 are nonnegative, c_1 denotes the biggest λ_t, and c_2 describes the curvature of the exponent curve. The variation tendency of λ_t is shown in Fig. 3. When $c_2 > 1$, the degree of smoothing in the shadow-free image has a larger difference between the umbra and the penumbra than in the situation where $c_2 \leq 1$. Hence, the shadow-free image can be smoothed in a spatially adaptive manner.

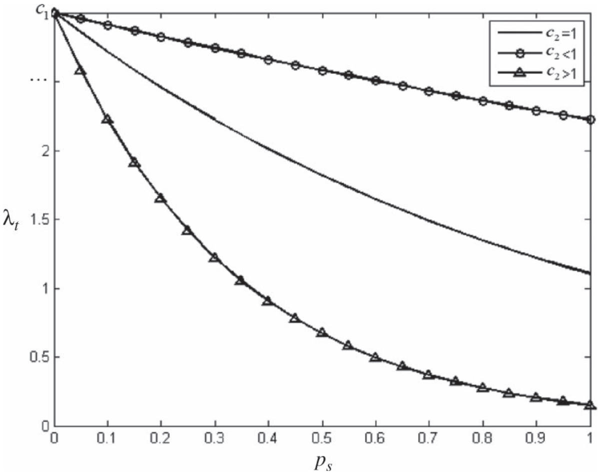

Fig. 3. Variation tendency of λ_t.

C. Improved NL Model: SA-NLSC

Shadows cast by tall manmade or natural objects are usually compound, particularly when the solar altitude is low. More than two types of land surfaces are usually contained in such a shadow, where the intensity attenuation varies according to the different physical properties of the different land surfaces. Thus, assuming the shadow scale to be spatially smooth in the whole shadow region is inappropriate, particularly when totally different land surfaces coexist in the same shadow. Therefore, we propose a spatially adaptive NL (SA-NL) regularization item for the shadow scale. SA-NL first clusters pixels in the shadow into m classes and then appends this clustered result to the NL operator on the shadow scale. The NL weights are calculated based on the clustered soft shadow, i.e.,

$$p_s^C = p_s \cdot C \tag{19}$$

where C denotes the clustered image, and

$$w_s^C(x,y) = \exp\left(- \frac{\left(G_a \left| p_s^C(x+.) - p_s^C(y+.) \right|^2 \right)(0)}{h^2} \right). \tag{20}$$

The inclusion of a clustered image increases the separability of the pixels. Moreover, it also makes sure that the weights are adaptively arranged, in accordance with the spatial properties. Pixels with similar structures but belonging to different classes are assigned with low weights. Only pixels belonging to the same class and with similar structures are assigned with high weights. This spatially adaptive behavior regionally smooths the shadow scale. It also avoids blurring the common boundaries of the adjacent classes and maintains the edges. Hence, the spatially adaptive NLSC (SA-NLSC) model can be expressed as

$$f = \arg\min_f \sum_{\Omega} \left[\|f - \hat{f}\|_{L2}^2 + \lambda_s \cdot \sum_{y\in x^{\mathrm{NL}}} (s(x) - s(y))^2 \times w_s^C(x,y) + \lambda_t \cdot \sum_{y\in x^{\mathrm{NL}}} (f(x) - f(y))^2 \, w_f(x,y) \right]. \tag{21}$$

Summarizing the main procedure of the proposed NL method, the algorithm flowchart is shown in Fig. 4. A synthesized image including two types of land surfaces is used. It should be noted that the dashed circle in the soft shadow marks the entire region of the shadow, including the umbra and the penumbra. The two curved surfaces beside the shadow scale are the 3-D representations of the results of NL and SA-NL. The NL result is entirely smooth, whereas the SA-NL result is regionally smooth, preserving the boundary that divides the two types of land surfaces.

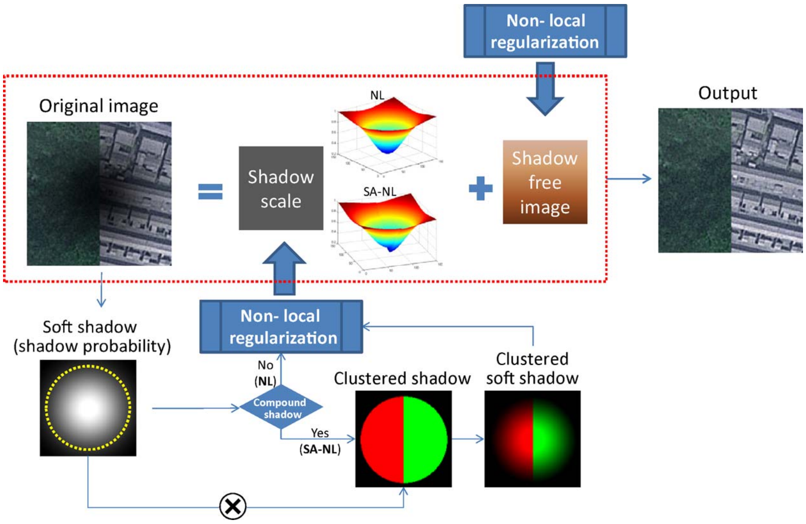

Fig. 4. Flowchart of the NL shadow removal method.

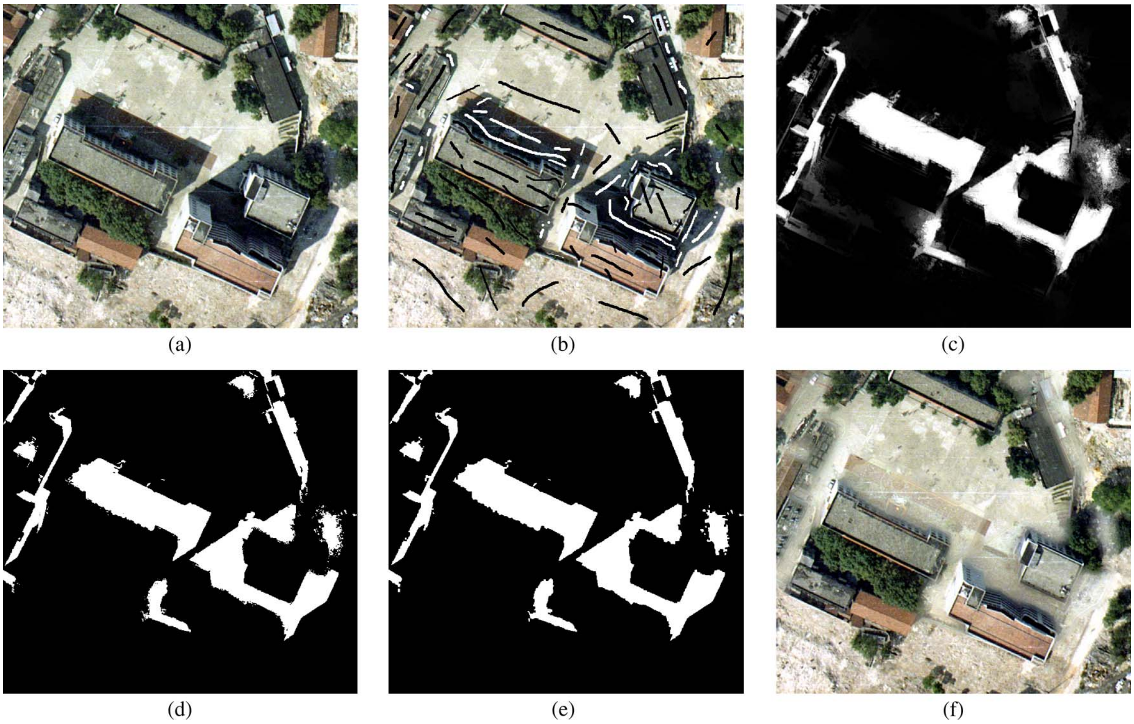
(a) (b) (c)
(d) (e) (f)

Fig. 5. Shadow removal results of the first aerial image. (a) Original image. (b) Marked (white) shadow and (black) nonshadow for soft SD. (c) Soft shadow. (d) Hard shadow. (e) Morphological filtered hard shadow. (f) Shadow-free result.

V. EXPERIMENTAL RESULTS

In this section, different aerial images, containing nonuniform, compound, and 0-pixel existing shadows, are employed to verify the ability of the proposed method. The halfway results and the shadow-free results of the five images are both presented. To evaluate the effect of this NL method, the results are compared with two other shadow removal methods.

A. Procedure and Results of the Proposed NL Method

Fig. 5 shows an aerial remote sensing image containing several buildings and trees. The cast shadows are almost all attributed to manmade buildings. For the detection of shadows by image matting, samples are first marked by scribbles in the original image, as shown in Fig. 5(b). White scribbles represent shadow regions, and black ones indicate absolute nonshadow regions. The matting result, as shown in Fig. 5(c), locates the shadows in a soft manner. Large entries indicate that the corresponding pixels have a high probability of belonging to the umbra; in contrast, small entries represent a low probability. Thus, the soft shadow is also named the shadow probability in this paper. From Fig. 5(c), it is shown that almost all the shadows have been extracted. Thresholding the soft shadow, we obtain the common hard shadow, i.e., a binary mask [see Fig. 5(d)]. Eliminating fragments and interstices by mathematical morphological open and close operators, the final hard shadow is shown in Fig. 5(e). As mentioned before,

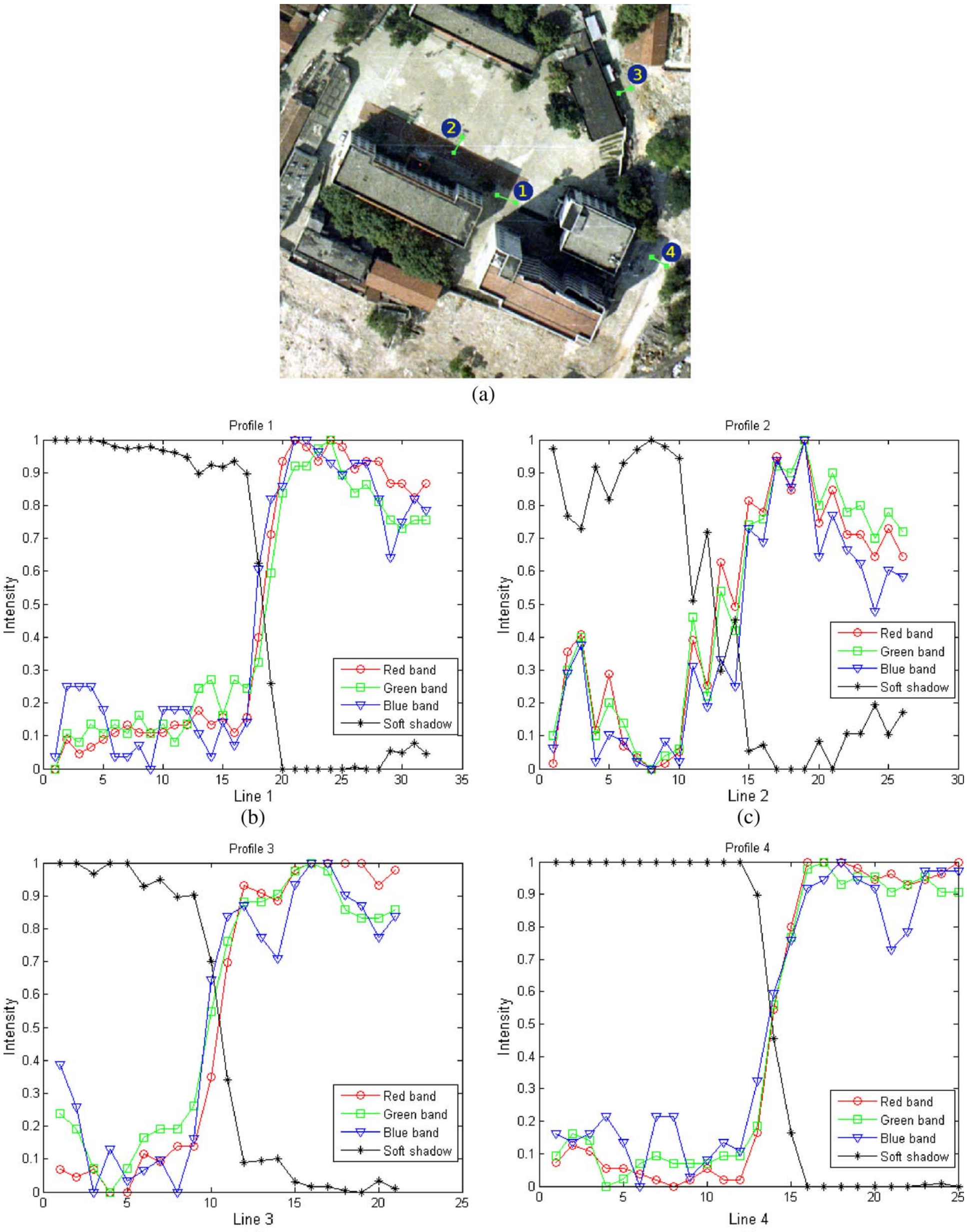

(a)

(b)

(c)

(d)

(e)

Fig. 6. Profiles of four selected penumbra parts. (a) Locations of the four parts in the original image. (b) Profile 1: 16th–20th pixel (the penumbra is located between the 16th and the 20th pixel). (c) Profile 2: 10th–17th pixel. (d) Profile 3: 8th–15th pixel. (e) Profile 4: 12th–16th pixel.

the existence of the penumbra implies that the intensity changes from the shadow to the nonshadow are gradual rather than abrupt. The soft shadow can depict the gradual intensity change in the penumbra properly, whereas the hard shadow is composed of two values, i.e., 0 and 1. To further investigate the validity of the soft shadow, we select four parts of the penumbras from the original image and display their profiles in the original image and the soft shadow (see Fig. 6). The four selected parts marked in the original image are presented in Fig. 6(a). Fig. 6(b)–(e) shows the corresponding profiles, respectively, in which entries in the original image and the soft shadow are normalized to the range of [0, 1]. By a visual measurement, the widths of the four penumbra are about 5, 8, 8, and 5 pixels, respectively. Correspondingly, the width of the soft-shadow edge contains the same number of pixels. The intensity changes in the first, third, and fourth penumbras are almost linear, as the adjacent shadow and nonshadow have identical land surfaces. Obviously, the tendency of the profile in the soft shadow complements the intensity change in the penumbra. When the intensity increases, the shadow probability declines. Even when compound land surfaces occur in the penumbra, as shown in the second penumbra profile in Fig. 6(c), the soft shadow also reflects the shadow probability. The shadow probability is valuable for processing nonuniform shadows in high-resolution aerial images. Fig. 5(f) shows the SC result of NLSC, as in (17), where $\lambda_s = 9$, λ_t is adaptively selected, $c_1 = 8$, and $c_2 = 2$. The result is visually pleasing, in which shadows are removed and the intensities of shadow pixels are enhanced to be consistent with the surrounding nonshadow pixels.

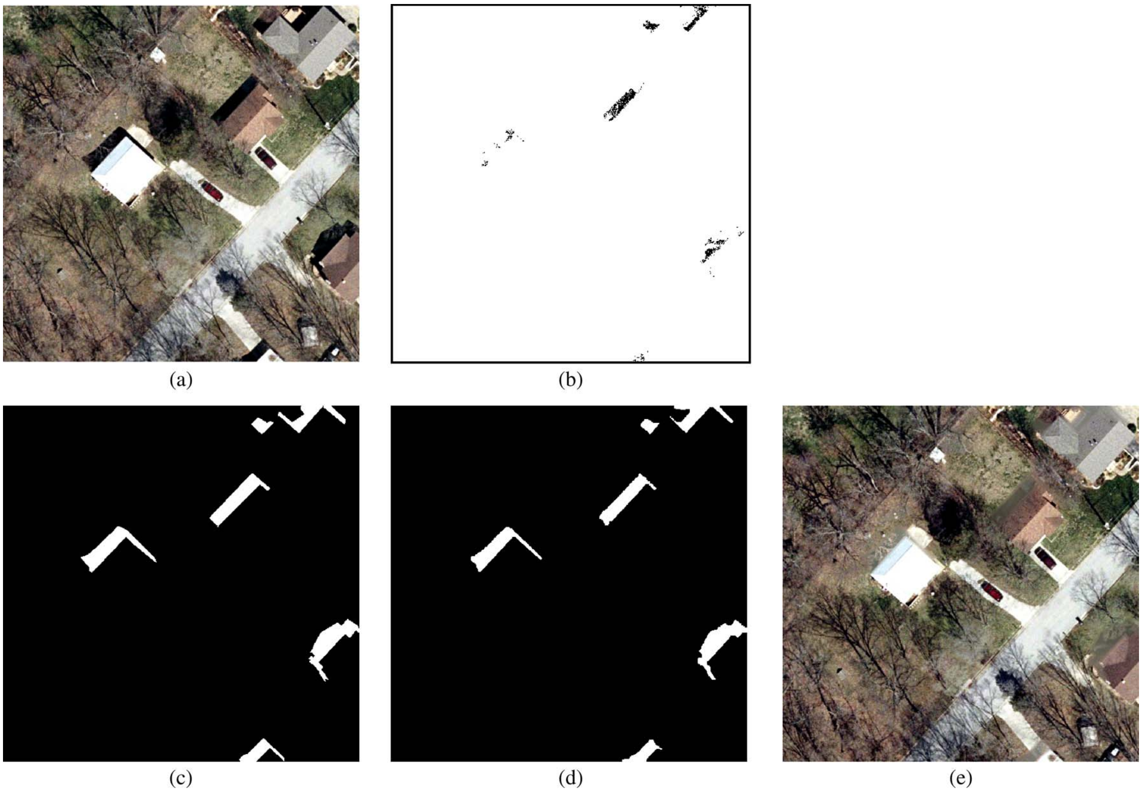

Fig. 7. First image from the UCF database: Building 1. (a) Original image. (b) Labeled 0-pixels. (c) Referenced hand-labeled shadow. (d) Detected hard shadow. (e) Shadow removal result.

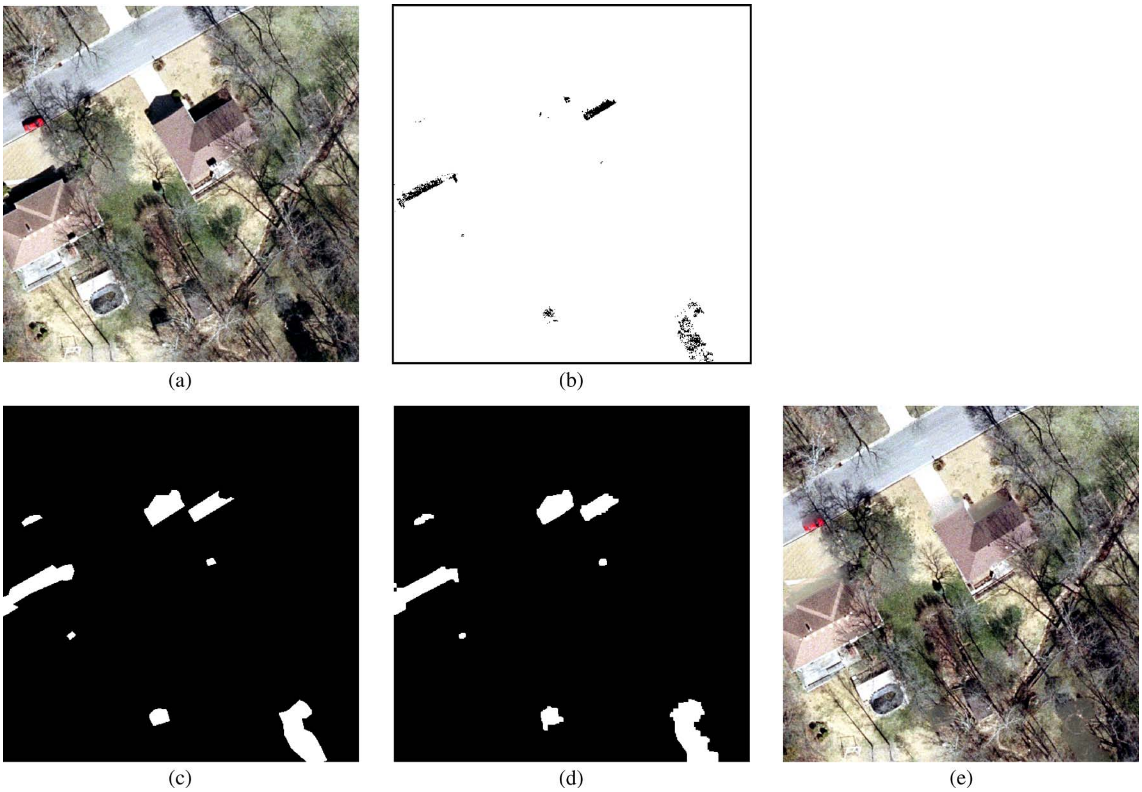

Fig. 8. First image from the UCF database: Building 1. (a) Original image. (b) Labeled 0-pixels. (c) Referenced hand-labeled shadow. (d) Detected hard shadow. (e) Shadow removal result.

As the intensities of pixels in the umbra mainly comes from the scattered environmental light, among the three visible channels, the blue light makes the biggest contribution, and the red light contributes little. Thus, 0-pixels almost all appear in the red channel. Figs. 7(a) and 8(a) are two shadowed aerial images from the database of the University of Central Florida,

TABLE I
SHADOW DETECTION ACCURACY MEASUREMENTS

	Recall ratio (%)	**Precision ratio (%)**
Building1	86.94	96.22
Building2	90.80	90.44

with referenced hand-labeled shadows. Figs. 7(b) and 8(b) label the 0-pixels in black and the other pixels in white. The proportions of 0-pixels are about 18.28% and 22.25% in these two images. In order to evaluate the detection accuracy, the hard shadows are obtained by thresholding the soft shadows resulting from the image matting. For a comparative analysis, the referenced shadows and the detected hard shadows are shown in Figs. 7(c) and (d) and 8(c) and (d). It can be observed that no shadow region is missed and that the shadow shapes are almost consistent with the referenced ones. To assess the detection result objectively, the recall ratios and the precision ratios of the two images are counted and listed in Table I. The statistics suggest that binary shadows with a high accuracy can be obtained by setting the appropriate thresholds on the soft shadows. Figs. 7(e) and 8(e) show the SC results of NLSC. It is shown that the shadows have been removed and no artifacts are generated. Both pixels with low intensities and zero intensities are enhanced using the NL neighbor pixels with high structural similarity. The impacts of the penumbra are counteracted by the NL operator based on the soft shadow. Meanwhile, the second NL operator constrains the general distribution of the shadow-free image. Thus, in the result, spatial smoothness is not only restored in the transitional part located between shadows and nonshadows but is also preserved inside the shadows.

The aforementioned experiments and analysis verify the following: 1) Image matting is applicable for detecting soft shadows, and the soft shadows can describe the distribution of shadows better than hard shadows. 2) The NL operator weighted by the soft shadows is useful for removing the penumbra of unitary shadows. 3) The adaptive parameter selection strategy solves the nonuniform shadow problem. It ensures that the second NL operator differently contributes among pixels and ensures the smoothness of the results. 4) The NLSC method performs well on the 0-pixels.

To investigate the effect of SA-NLSC, another two aerial images with both compound and nonuniform shadows are used in the following experiments (see Figs. 9–12). Two or more land surfaces are included in the compound shadows. Taking Fig. 9, for instance, the number 1 shadow labeled in Fig. 9(b) covers two types of land surfaces, i.e., lawn and bare soil. The intensity attenuation caused by the same shadow varies between different types of pixels. Soft shadows of the two aerial images, as shown in Figs. 9(b) and 11(b), depict the nonuniform property of each shadow. Results of the NLSC method using (17) are presented in Figs. 9(c) and 11(c). It can be seen that the shadows are almost removed, but some unexpected artifacts in the penumbra are generated, as the enlarged clipped regions shown in Figs. 10(a) and (b) and 12(a) and (b). Moreover, some color cast and blur appear in the restored shadow-free image [see Figs. 10(c) and 12(c)]. If a larger λ_t value is assigned, the restored shadow-free image will be more seriously blurred and color cast, and intrinsic edges in the shadow will be blurred, as Fig. 12(a) shows. These defects can be attributed to the lack of knowledge about the land surfaces. The shadow scale of the compound shadow should be regionally smooth, according to the different land surfaces, rather than generally smooth. Otherwise, even the soft shadow and the adaptive regularization parameter cannot yield a pleasing result. Therefore, the SA-NL method is derived to treat compound shadows, as interpreted in Section IV.

We divide shadows by area into large shadows and small shadows. Small shadows can be considered unitary, such as the number 2 shadow in Fig. 9, while large shadows, which are usually composed of more than 10 000 pixels, are regionally treated, according to the spatial properties. Considering the high spatial resolution of aerial images and the height of the buildings in our experimental data, two or three types of land surfaces are clustered in the large shadows. Usually, we determine the cluster number by visual interpretation. Taking Fig. 9, for instance, two classes are clustered by k-means in the large shadows, and the class map C is shown in Fig. 9(e). Different classes in each shadow are marked by different colors. Considering the nonuniform nature of the cast shadows, the shadow probability represented by the soft shadow is combined with the class map to construct the clustered soft shadow, as shown in Fig. 9(f). A new NL weight is calculated based on p_s^C and applied in the NL regularization term for the shadow scale. The result of this SA-NL method is presented in Fig. 9(d), and the three images in Fig. 10(d)–(f) are the enlarged partial regions clipped from Fig. 9(d). Compared with the result of the original NLSC method shown in Figs. 9(c) and Fig. 10(a)–(c), the unexpected artifacts (fake edges) are eliminated, and the true color is restored in the SA-NLSC result. The same operations are performed in Fig. 11(a). Three classes are clustered in the large shadows, and the results are shown in Fig. 11(d)–(f) and Fig. 12(d)–(f). From the enlarged regions shown in Fig. 12(d)–(f), we can see that, aside from eliminating artifacts and regulating cast color, the spatially adaptive method also maintains the intrinsic edges well.

The experiments on these two aerial images validate the effect of the SA-NL method. The regional smoothness of the shadow scale is an effective way to process the compound shadows. Meanwhile, with the assistance of the adaptive regularization parameter, the nonuniform nature of each shadow is given sufficient consideration, which eliminates the fake edges. Therefore, the combination of the three items in the energy function (the fidelity item and the two NL regularized items) can yield satisfactory shadow-free results.

B. Comparative Analysis

To further verify the effect of the proposed NL method for shadow removal, we compare the shadow removal results with the results of two other methods, i.e., Tsai's method [2] and the Poisson method [16]. Using the same SD method, the shadow removal results of these three methods are presented in Fig. 13. Three obvious defects exist in the results of Tsai's

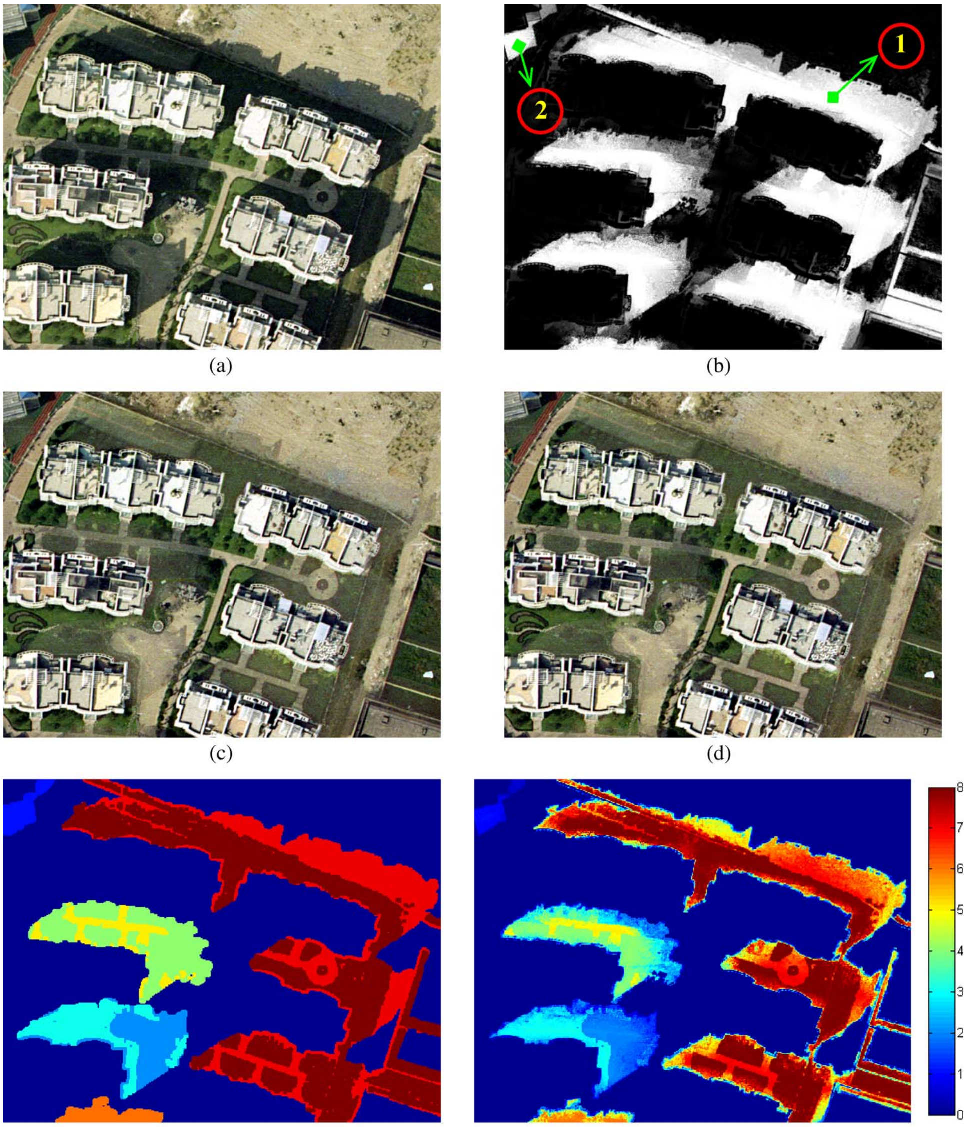

(a) (b)

(c) (d)

(e) (f)

Fig. 9. Results of the first image with compound shadows. (a) Original image. (b) Detected soft shadow. (c) Shadow-free result of NLSC. (d) Shadow-free result of SA-NLSC. (e) Clustered map of shadows. (f) Clustered soft shadow.

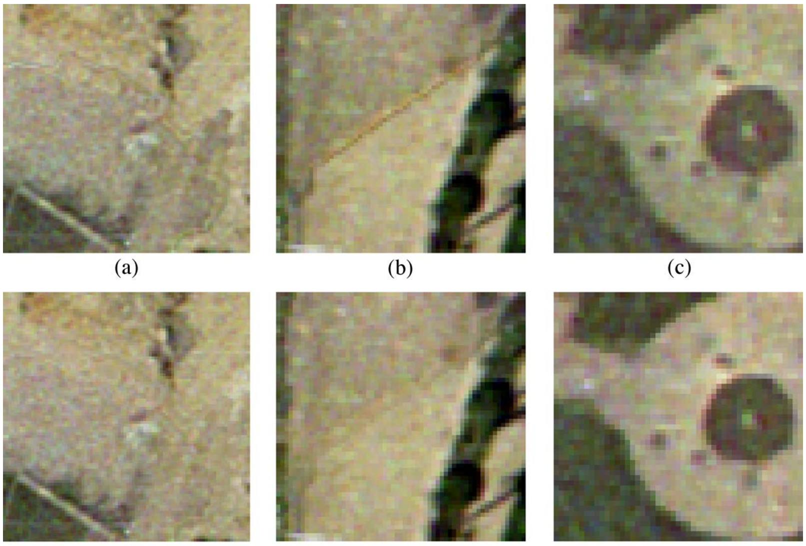

(a) (b) (c)

(d) (e) (f)

Fig. 10. Enlarged regions clipped from Fig. 9(c) and (d). (a)–(c) Three regions clipped from Fig. 9(c). (d)–(f) Three regions clipped from Fig. 9(d).

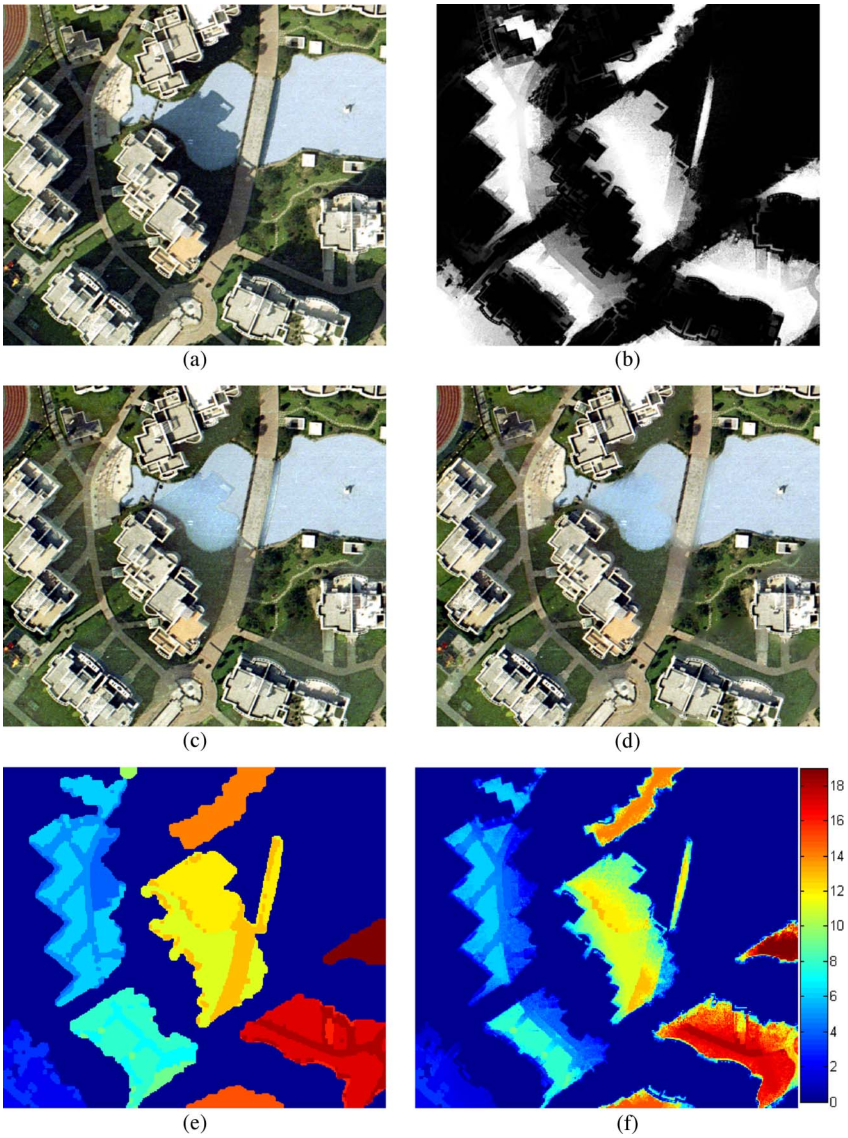
(a) (b) (c) (d) (e) (f)

Fig. 11. Results of the second image with compound shadows. (a) Original image. (b) Soft shadow. (c) Shadow-free result of NLSC. (d) Shadow-free result of SA-NLSC. (e) Clustered map of shadows. (f) Clustered soft shadow.

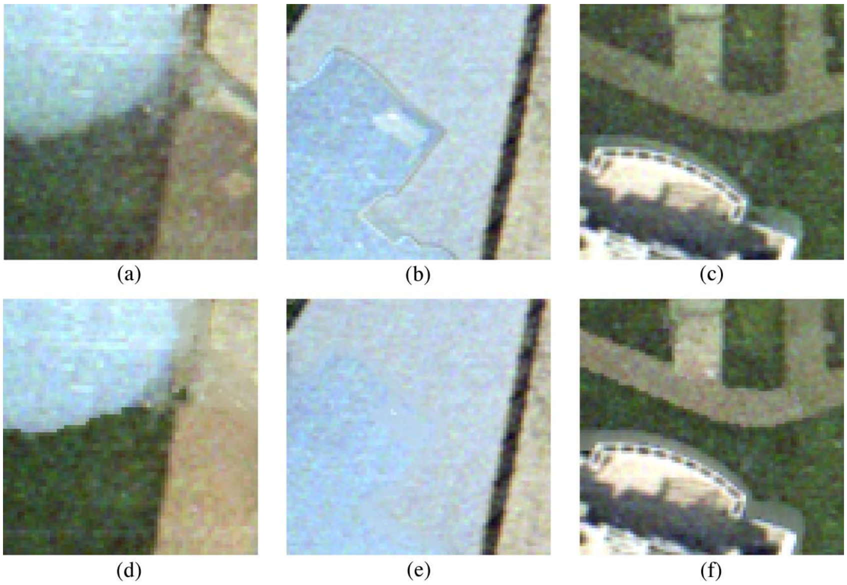
(a) (b) (c) (d) (e) (f)

Fig. 12. Enlarged regions clipped from Fig. 11(c) and (d). (a)–(c) Three regions clipped from Fig. 11(c). (d)–(f) Three clipped regions from Fig. 11(d).


(a) (b) (c) (d) (e) (f) (g) (h) (i) (j) (k) (l) (m) (n) (o)

Fig. 13. Results of the three shadow removal methods. Results of (left column) the proposed method, (middle column) Tsai's method, and (right column) the Poisson method.

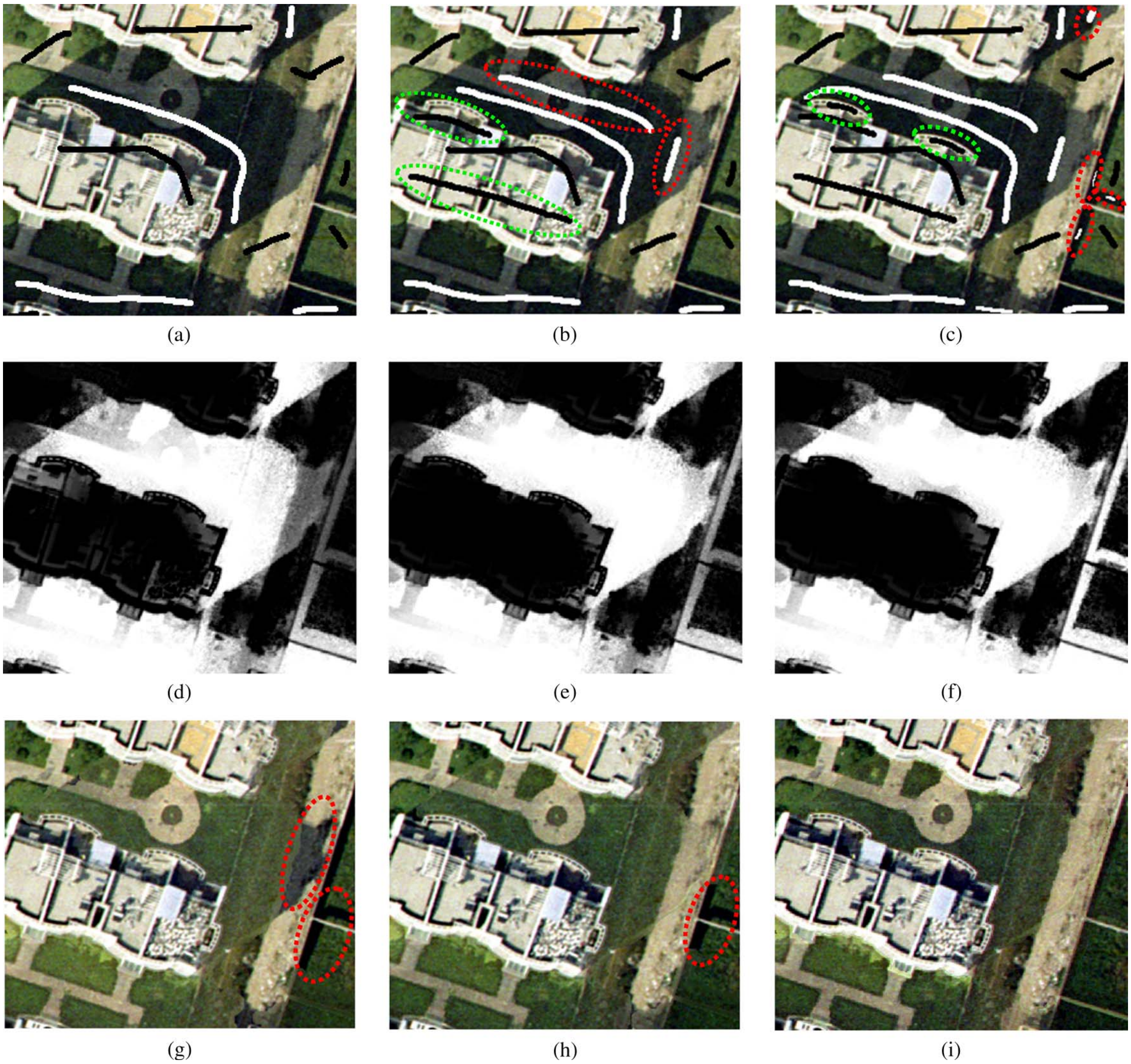

Fig. 14. Results of different initial markings. (a) Image with the least markings. (b) Image with an average number of markings. (c) Image with the most markings. (d)–(f) Detected soft shadows for (a)–(c). (g)–(i) Shadow compensation results based on the SD results in (d)–(f).

method: 1) artifacts appear in the original penumbra region, as the images in the middle column of Fig. 13 show; 2) shadow pixels are overexposed, causing an amount of noise in the results, particularly in the bright shadow pixels; and (3) shadow pixels with very low or even zero intensities are inaccurately reconstructed. Most 0-pixels are rendered red, as shown in Fig. 13(e) and (h), and dark-shadow pixels are rendered green, as Fig. 13(b) shows. In contrast, in the proposed method, substituting the soft shadow for the hard shadow avoids the emergence of artifacts, controlling the spatial smoothness of the result preserves the total exposure, and the fidelity item ensures the approximation of restored 0-pixels to the true values. The results of the proposed method are shown in the left column of Fig. 13.

Examining the results in the right column in Fig. 13, it can be seen that the Poisson method handles penumbras well, avoiding artifacts. One defect, as with Tsai's method, is the failure to handle 0-pixels. Serious errors appear in Fig. 13(f) and (i). Another shortcoming of the Poisson method is that it adjusts the whole scene without maintaining nonshadows. Thus, a color cast often happens in the whole image, particularly when shadows are very dark, such as in Fig. 13(c), (f), and (i). When the shadows are light, the results of the Poisson method are acceptable, such as in Fig. 13(l) and (o). The problem is that the contrast of the restored shadow regions is lower than that of nonshadow regions. This can be attributed to the lack of knowledge about the physical properties of the different land surfaces. Results of the SA-NLSR method exhibit clearer edges and a more natural color.

Summarizing the experimental results and the aforementioned discussion, the nonlocal regularized shadow removal (NLSR) method outperforms the other two methods and solves the four main problems encountered with shadow removal in aerial images. Even when the shadow is compound, nonuniform, includes 0-pixels, and is affected by the penumbra, NLSR yields a shadow-free result with clear textures and regularized color. However, it should still be noted that selecting the appropriate regularization parameters λ_s and c_1 is essential for the performance of the proposed method, particularly in avoiding unexpected artifacts and noise.

C. Discussion on Initial Markings and Model Parameters

Two factors, the initial markings and the model parameters, have a significant effect on the SD and the SC.

Here, we investigate the influence of the initial markings on the SD by undertaking experiments on a subsection of the first image with compound shadows, as shown in Fig. 14. There are some rules that should be obeyed when marking scribbles. For the shadows, first, place the white scribbles as close as possible to the obstacle because those regions contain the most likely shadow pixels in the nonuniform shadow, as Fig. 14(a) shows. Second, try to cover all the different kinds of land surfaces [see the white scribbles in Fig. 14(b) emphasized by the red dashed ellipse]. For the nonshadows, mark all the regions that you do not want to mix with the shadows. In this paper, we are only concerned about the shadows cast on the ground; thus, any self-shadows located on buildings and roofs should be excluded from the detection result. With an increase in black marks, as the green dashed ellipses shown in Fig. 14(b) and (c), less self shadows are mixed in the soft SD result [see Fig. 14(d)–(f)]. Moreover, the white scribbles located near the right margin in Fig. 14(c) increase the entries of the corresponding pixels in Fig. 14(f). The shadow-removed images based on these three different soft shadows are presented in Fig. 14(g)–(i). The results suggest that accurate SD results yield satisfactory shadow removal results. Therefore, in order to obtain an ideal detection result, we usually take the soft SD as an iterative process. First, mark the black and white scribbles following the aforementioned rules, and evaluate the detected soft shadow by visual assessment. Then, add or remove the marks to increase the precision of the detection result until most pixels are assigned the correct shadow probabilities.

In the NL regularized SC model, three parameters affect the result from the following different aspects: λ_s controls the smoothness of the shadow scale, i.e., a larger λ_s results in a smoother shadow scale and a sharper result; c_1 is directly positively related to the smoothness of the shadow removal result; and c_2 controls the variation of λ_t between pixels with different shadow probabilities, i.e., a larger c_2 leads to a larger discrepancy. As there is no ground truth available, it is hard to assess the shadow removal results quantitatively. Visual assessment plays the significant role in parameter determination. It is concluded, based on our experiments, that shadow removal results become stable when λ_s and c_2 are large enough, where c_2 should usually be greater than 1; and the method is highly sensitive to c_1, i.e., a too large c_1 will cause serious blur in the final result, and it usually should be less than 1 for 8-bit data.

VI. CONCLUSION

A novel adaptive shadow removal method using NL operators has been developed for aerial images. Image matting has been used for effectively detecting soft shadows, and the NL regularized SC yields satisfactory shadow-free results. Soft shadows are demonstrated as being fit for depicting penumbras and nonuniform shadows. The fidelity item ensures the approximation of restored shadow pixels to the ground truth. The first NL operator, regularizing the shadow scale, preserves the edges and the textures in the shadow regions. Using k-means clustering to distinguish different land surfaces restores clear boundaries in compound shadows. Combining the first NL operator with the second NL operator (weighted by an adaptive regularization parameter) avoids oversmoothing in the umbra and undersmoothing in the penumbra.

Results of the proposed NL regularized method have been compared with Tsai's method and the Poisson method. Considering four different aspects (edges, textures, color, and artifacts), our method outperforms the other two methods. In our future research, we would like to extend the isotropic NL operator to an advanced anisotropic operator for better restoration results.

REFERENCES

[1] A. Makarau, R. Richter, R. Muller, and P. Reinartz, "Adaptive shadow detection using a blackbody radiator model," *IEEE Trans. Geosci. Remote Sens.*, vol. 49, no. 6, pp. 2049–2059, Jun. 2011.

[2] V. J. D. Tsai, "A comparative study on shadow compensation of color aerial images in invariant color models," *IEEE Trans. Geosci. Remote Sens.*, vol. 44, no. 6, pp. 1661–1671, Jun. 2006.

[3] P. Sarabandi, F. Yamazaki, M. Matsuoka, and A. Kiremidjian, "Shadow detection and radiometric restoration in satellite high resolution images," in *Proc. IGARSS*, Sep. 2004, vol. 6, pp. 3744–3747.

[4] K. L. Chung, Y. R. Lin, and Y. H. Huang, "Efficient shadow detection of color aerial images based on successive thresholding scheme," *IEEE Trans. Geosci. Remote Sens.*, vol. 47, no. 2, pp. 671–682, Feb. 2009.

[5] E. Arbel and H. Hel-Or, "Shadow removal using intensity surfaces and texture anchor points," *IEEE Trans. Pattern Anal. Mach. Intell.*, vol. 33, no. 6, pp. 1202–1216, Jun. 2011.

[6] L. Lorenzi, F. Melgani, and G. Mercier, "A complete processing chain for shadow detection and reconstruction in VHR images," *IEEE Trans. Geosci. Remote Sens.*, vol. 50, no. 9, pp. 3440–3452, Sep. 2012.

[7] T. P. Wu, C. K. Tang, M. S. Brown, and H. Y. Shum, "Natural shadow matting," *ACM Trans. Graph.*, vol. 26, no. 2, pp. 8:1–8:21, Jun. 2007.

[8] X. Huang and L. Zhang, "Morphological building/shadow index for building extraction from high-resolution imagery over urban areas," *IEEE J. Sel. Topics. Appl. Earth Observ. Remote Sens.*, vol. 5, no. 1, pp. 161–172, Feb. 2012.

[9] W. Liu and F. Yamazaki, "Object-based shadow extraction and correction of high-resolution optical satellite images," *IEEE J. Sel. Topics Appl. Earth Observ. Remote Sens.*, vol. 5, no. 4, pp. 1296–1302, Aug. 2012.

[10] A. Levin, D. Lischinski, and Y. Weiss, "A closed-form solution to natural image matting," *IEEE Trans. Pattern Anal. Mach. Intell.*, vol. 30, no. 2, pp. 228–242, Feb. 2008.

[11] F. Yamazaki, W. Liu, and M. Takasaki, "Characteristics of shadow and removal of its effects for remote sensing imagery," in *Proc. IGARSS*, Jul. 2009, vol. 4, pp. IV-426–IV-429.

[12] Y. Li, P. Gong, and T. Sasagawa, "Integrated shadow removal based on photogrammetry and image analysis," *Int. J. Remote Sens.*, vol. 26, no. 18, pp. 3911–3929, Sep. 2005.

[13] R. Mcfeely, C. Hughes, E. Jones, and M. Glavin, "Removal of non-uniform complex and compound shadows from textured surfaces using adaptive directional smoothing and the thin plate model," *IET Image Process.*, vol. 5, no. 3, pp. 233–248, Apr. 2011.

[14] E. Arbel and H. Hel-Or, "Texture-preserving shadow removal in color images containing curved surfaces," in *Proc. IEEE CVPR*, Jun. 2007, pp. 1–8.

[15] G. D. Finlayson, M. S. Drew, and C. Lu, "Entropy minimization for shadow removal," *Int. J. Comput. Vis.*, vol. 85, no. 1, pp. 35–57, Oct. 2009.

[16] G. D. Finlayson, S. D. Hordley, C. Lu, and M. S. Drew, "On the removal of shadows from images," *IEEE Trans. Pattern Anal. Mach. Intell.*, vol. 28, no. 1, pp. 59–68, Jan. 2006.

[17] L. Xu, F. Qi, and R. Jiang, "Shadow removal from a single image," in *Proc. 6th Int. Conf. Intell. Syst. Des. Appl.*, Oct. 2006, vol. 2, pp. 1049–1054.

[18] G. Peyré, S. Bougleux, and L. Cohen, "Non-local regularization of inverse problems," in *Proc. ECCV*, 2008, pp. 57–68.

[19] A. Buades, B. Coll, and J. M. Morel, “A non-local algorithm for image denoising,” in *Proc. IEEE CVPR*, 2005, vol. 2, pp. 60–65.

[20] Y. Lou, X. Zhang, S. Osher, and A. Bertozzi, “Image recovery via nonlocal operators,” *J. Sci. Comput.*, vol. 42, no. 2, pp. 185–197, Feb. 2010.

[21] G. Gilboa and S. Osher, “Nonlocal operators with applications to image processing,” *Multiscale Model. Simul.*, vol. 7, no. 3, pp. 1005–1028, 2008.

[22] J. Mairal, F. Bach, J. Ponce, G. Sapiro, and A. Zisserman, “Non-local sparse models for image restoration,” in *Proc. 12th ICCV*, 2009, pp. 2272–2279.

[23] P. M. Dare, “Shadow analysis in high-resolution satellite imagery of urban areas,” *Photogramm. Eng. Remote Sens.*, vol. 71, no. 2, pp. 169–177, 2005.

[24] R. Kimmel, M. Elad, D. Shaked, K. Keshet, and I. Sobel, “A variational framework for retinex,” *Int. J. Comput. Vis.*, vol. 52, no. 1, pp. 7–23, Apr. 2003.

[25] M. Bertalmio, V. Caselles, and E. Provenzi, “Issues about retinex theory and contrast enhancement,” *Int. J. Comput. Vis.*, vol. 83, no. 1, pp. 101–119, Jun. 2009.

[26] H. Li, L. Zhang, and H. Shen, “A perceptually inspired variational method for the uneven intensity correction of remote sensing images,” *IEEE Trans. Geosci. Remote Sens.*, vol. 50, no. 8, pp. 3053–3065, Aug. 2012.

[27] E. Reinhard, M. Adhikhmin, B. Gooch, and P. Shirley, “Color transfer between images,” *IEEE Comput. Graph. Appl.*, vol. 21, no. 5, pp. 34–41, Sep./Oct. 2001.

[28] F. L. Gadallah, F. Csillag, and E. J. M. Smith, “Destriping multisensor imagery with moment matching,” *Int. J. Remote Sens.*, vol. 21, no. 12, pp. 2505–2511, 2000.

[29] H. Shen and L. Zhang, “A MAP-based algorithm for destriping and inpainting of remotely sensed images,” *IEEE Trans. Geosci. Remote Sens.*, vol. 47, no. 5, pp. 1492–1502, May 2009.

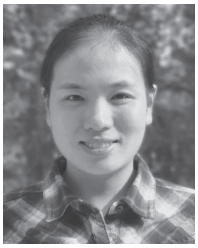

Huifang Li received the B.S. degree in geographical information science from China University of Mining and Technology, Xuzhou, China, in 2008. She is currently working toward the Ph.D. degree in the State Key Laboratory of Information Engineering in Surveying, Mapping, and Remote Sensing, Wuhan University, China.

Her research interests include variational methods, image processing, and dehazing and deshadowing of remote sensing images.

Liangpei Zhang (M’06–SM’08) received the B.S. degree in physics from Hunan Normal University, Changsha, China, in 1982, the M.S. degree in optics from the Xi’an Institute of Optics and Precision Mechanics of Chinese Academy of Sciences, Xi’an, China, in 1988, and the Ph.D. degree in photogrammetry and remote sensing from Wuhan University, Wuhan, China, in 1998.

He is currently the Head of the Remote Sensing Division, State Key Laboratory of Information Engineering in Surveying, Mapping, and Remote Sensing, Wuhan University. He is also a “Changjiang Scholar” Chair Professor appointed by the Ministry of Education, China. He has more than 260 research papers and five patents. He is now Principal Scientist for the China State Key Basic Research Project (2011–2016) appointed by the Ministry of National Science and Technology of China to lead the remote sensing program in China. His research interests include hyperspectral remote sensing, high-resolution remote sensing, image processing, and artificial intelligence.

He regularly serves as a Cochair of the series SPIE (The International Society for Optical Engineering) Conferences on Multispectral Image Processing and Pattern Recognition, Conference on Asia Remote Sensing, and many other conferences. He edits several conference proceedings, issues, and the Geoinformatics Symposiums. He also serves as an Associate Editor of the IEEE TRANSACTIONS ON GEOSCIENCE AND REMOTE SENSING, the International Journal of Ambient Computing and Intelligence, the International Journal of Image and Graphics, the International Journal of Digital Multimedia Broadcasting, the Journal of Geospatial Information Science, and the Journal of Remote Sensing. He is a Fellow of the Institution of Electrical Engineers, an Executive Member (Board of Governor) of the China National Committee of International Geosphere–Biosphere Programme, an Executive Member for the China Society of Image and Graphics, and others.

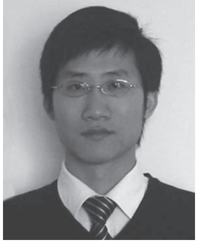

Huanfeng Shen (M’10) received the B.S. degree in surveying and mapping engineering and the Ph.D. degree in photogrammetry and remote sensing from Wuhan University, Wuhan, China, in 2002 and 2007, respectively.

Since July 2007, he has been with the School of Resources and Environmental Science, Wuhan University, where he is currently a Professor and is also with the State Key Laboratory of Information Engineering in Surveying, Mapping, and Remote Sensing. His current research interests include image processing, remote sensing application, data fusion, and data assimilation.